IEEE Photonics Journal
An IEEE Photonics Society Publication

Open Access

A Moiré-Based Four-Channel Focusing and Leveling Scheme for Projection Lithography

Volume 6, Number 4, August 2014

Chengliang Di
Wei Yan
Song Hu
Yanli Li
Didi Yin
Yan Tang
Junmin Tong

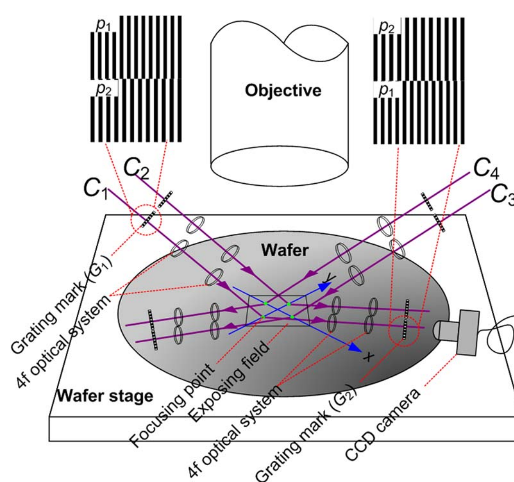

DOI: 10.1109/JPHOT.2014.2332559
1943-0655 © 2014 IEEE

IEEE photonics SOCIETY

IEEE

A Moiré-Based Four-Channel Focusing and Leveling Scheme for Projection Lithography

Chengliang Di,[1,2] Wei Yan,[1] Song Hu,[1] Yanli Li,[1] Didi Yin,[2] Yan Tang,[1] and Junmin Tong[3]

[1]State Key Laboratory of Optical Technologies for Microfabrication, Institute of Optics and Electronics, Chinese Academy of Sciences, Chengdu 610209, China
[2]University of Chinese Academy of Sciences, Beijing 100049, China
[3]Xuchang Vocational and Technical College, Xuchang 461000, China

DOI: 10.1109/JPHOT.2014.2332559
1943-0655 © 2014 IEEE. Translations and content mining are permitted for academic research only. Personal use is also permitted, but republication/redistribution requires IEEE permission. See http://www.ieee.org/publications_standards/publications/rights/index.html for more information.

Manuscript received May 15, 2014; revised June 10, 2014; accepted June 16, 2014. Date of publication June 24, 2014; date of current version July 8, 2014. This work was supported by the National Natural Science Foundation of China under Grants 61274108, 61204114, and 61376110. Corresponding author: Chengliang Di (e-mail: chengliangdi@163.com).

Abstract: Focusing and leveling are two imperative processes to adjust the wafer onto the ideal focal plane of projection lithography tools. Based on moiré fringes formed by particularly designed dual-grating marks, the four-channel focusing and leveling scheme is proposed and demonstrated. These relationships between the tilted amount of wafer, the vertical defocusing amount, and the phase distributions of moiré fringes are deduced. A single-channel experimental setup is constructed to verify the performances of proposed method. Results indicate that the tilted amount and the vertical defocusing amount can be precisely detected with accuracy at 10^{-4} rad and several nanometers level, respectively, and therefore meet the demand of the high-demanding focusing and leveling processes.

Index Terms: Moiré fringes, focusing and leveling, fringe analysis, lithography.

1. Introduction

Focusing and leveling have always been playing critical roles in a typical photolithographic system like stepper that operates in projection lithography [1], [2]. Along with the pursuit of higher and higher lithographic resolution, the exposing wavelength decreases while the numerical aperture (NA) increases, which results in a drastic shrink of the depth of focus (DOF) [3]–[5]. To transfer the mask patterns clearly and precisely onto the photoresist, full advantages of the restricted DOF should be taken in focusing and leveling processes.

Taking into account the narrow space between projection objective and the wafer, the focusing process (generally, the focusing process is the core issue of the focusing and leveling processes) was always performed by constructing a triangular optical path to transform the up and down fluctuations of the horizontal wafer into the displacement of reflected light [6]–[13]. For the first time, a slot like mark based technique, that detects the shift of slot caused by vertical movement of the wafer, was proposed by Suwa [6]. Then, in [7]–[9], it is further demonstrated that the heights at multi-points can be obtained by utilizing the slot or pinhole array marks so that the focusing and leveling could be achieved simultaneously using those heights data. However,

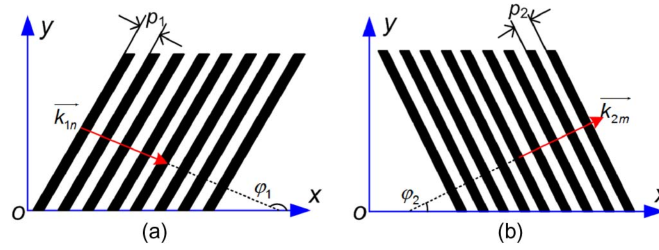

Fig. 1. (a) Grating g_1 with period p_1 whose IPT angle is φ_1. (b) Grating g_2 with period p_2 whose IPT angle is φ_2.

these methods rely heavily on the image processing algorithms and they can be easily affected by the slight machining errors of focusing marks. Although many current mature optical homodyne or heterodyne focusing methods, with improved focusing accuracy, emerged by detecting the intensity or phase of interferential beams [10]–[13], they undergo complex optics and susceptibilities to environment. Moreover, our previous work had preliminarily inferred that moiré fringes are able to provide better focusing solution with advantage of higher accuracy [14]–[16]; nevertheless, previous work mainly focused on the measurement of relative linear displacement between the objective and the wafer with assuming that the wafer is horizontal without any tilt [14].

Unfortunately, the wafer tilts, which tend to be unavoidable [17]–[19], result in deformations of the moiré fringes, also it can significantly influence the demodulation of defocusing amount. Hence, further studies that verify the feasibility of applying the moiré-based method on a tilted wafer are fair essential. With adequate considerations among wafer tilts, vertical defocusing amount and moiré fringes distributions, this paper aims to put forward the moiré-based four-channel measurement scheme. The coupling relationships between those three parts are explored in the terms of theoretical derivations, simulations and experiments. Final results indicate that the moiré-based method is competent to detect wafer tilts as well as the vertical defocusing amount with high accuracy.

2. Theory: Fundamental Model

2.1. Transmittance Model of Superposed Gratings

Illuminating the superposed periodic structures like gratings with the monochromic planar wave, the moiré fringes emerge as a physical phenomenon that the monochromic planar wave diffracts twice through the gratings. Considering a linear grating whose grooves extend along the x axis, at the incidence of a planar wave, the field distribution on xoy or grating plane is expressed as a combination of the multi-diffractive orders [20]

$$E(x,y,0)=\sum_{n=-\infty}^{+\infty}A_n\exp\left(j\frac{2\pi}{\lambda}x\sin\theta_n\right)=\sum_{n=-\infty}^{+\infty}A_n\exp(j\overrightarrow{k_n}\cdot x) \quad (1)$$

where A_n and θ_n are the coefficient and diffractive angle of the nth diffractive order, respectively, and λ is the wavelength of the incident light, and $\overrightarrow{k_n}=2\pi nf_0$ is the transverse vector of nth diffractive order, and f_0 is the fundamental frequency of the grating. Equation (1) implies that the intensity distribution is just related to the period of the grating and it is independent from the incident wavelength. This can also be concluded as that the spatial frequency of diffractive order is in accord with the spatial frequency of grating [16].

In order to generate moiré fringes, two in-plane twisted (IPT) linear gratings g_1 and g_2, shown in Fig. 1, are overlapped and illuminated by a monochromic planar wave. At the rear surface of g_1, the diffractive orders penetrate through the second grating g_2 and diffract again.

The intensity distributions of these second diffraction waves are determined by the joint impacts of g_1 and g_2. After the dual-diffraction, the multi-diffractive orders jointly combine the moiré distributions [21] as

$$E(x,y,0) = \sum_{n=-\infty}^{+\infty}\sum_{m=-\infty}^{+\infty} A_n B_m \exp\left(\overrightarrow{k_{n,m}}\cdot(x,y)\right) = \sum_{(n,m)} A_n B_m \exp(\overrightarrow{k_{1n}}+\overrightarrow{k_{2m}})\cdot(x,y)$$
$$= \sum_{(n,m)} A_n B_m \exp\{i2\pi[(nf_1\cos\varphi_1 + mf_2\cos\varphi_2)x + (nf_1\sin\varphi_1 + mf_2\sin\varphi_2)y]\} \quad (2)$$

where A_n and B_m are the corresponding coefficients of the nth and mth diffractive orders, $\overrightarrow{k_{1n}}$ and $\overrightarrow{k_{2m}}$ are the corresponding transverse vectors, and $\overrightarrow{k_{n,m}}$ is termed as the dual-diffractive transverse vector which means that the nth diffractive order of g_1 performs a mth diffraction at the surface of g_2.

Considering a special case in (2), when $m=-n=1$ and $\varphi_1=\varphi_2=0^\circ$, the most distinguished order $(1,-1)$, with small diffractive angle, constitutes the lowest frequency moiré fringes as

$$E_{(1,-1)}(x,y,0) = C_1\exp[i2\pi(f_1-f_2)x] \quad (3)$$

where C_1 is the coefficient of the first order of the moiré fringes. And the period of moiré fringes can be easily expressed as

$$p_{moire} = \frac{1}{f_1-f_2} = \frac{p_1\cdot p_2}{|p_1-p_2|}. \quad (4)$$

Obviously, the period of moiré fringes is much larger than that of g_1 and g_2. Therefore, a tiny transverse shift between g_1 and g_2 can be illustrated by the prominent shift of moiré fringes. Just because of this intrinsical property, the moiré-based method could achieve high performances in focusing and leveling.

2.2. The Four-Channel Focusing and Leveling Scheme

Due to the wafer warpage, thermal expansion and adsorption strain [22], overlay errors might be easily introduced leading to locally uncertain wafer tilts. Therefore, focusing and leveling are generally performed over a field by field basis where heights at several symmetrical points are measured in one exposing field. The mean value of these heights stands for the central height of the exposing field while the gradients between all different points imply the wafer tilts around x or y axis.

Fig. 2 illustrates the space and top-view diagrams of the four-channel focusing and leveling scheme, where the four focusing points locate symmetrically on both the x and y axis. The specially designed grating marks are shown in the upper-left and upper-right of Fig. 2(a). Two sets of gratings with close periods p_1 and p_2 ($r = p_1/p_2 = 8:10$) combine the mark G_1, G_2 can be obtained if the assembling of G_1 is reversed. Height (defocusing amount) at each focusing point can be obtained through analyzing the moiré fringes generated from corresponding channel. As the four channels (C_1, C_2, C_3, and $C_{4]}$,) are basically the same with each other, analyzing on a single-channel should substantially reflect the whole scheme.

As we can see, the single-point focusing scheme, e.g., C_1 extracted from Fig. 2, is detailed in Fig. 3. At an incident angle θ (generally $\theta >= 70^\circ$, to form a grazing incidence), G_1 is imaged as S_1 by the left 4f system. If specula reflection occurs, S_1 is mirrored as S_2. And then S_2 is imaged by the right 4f system as G_1'. Since the 4f optical systems are designed as dual-telecentric structures, which are characterized by large DOF and constant magnification, G_1' could perfectly superpose with G_2 generating moiré fringes shown in Fig. 4(a). When the wafer defocuses (the

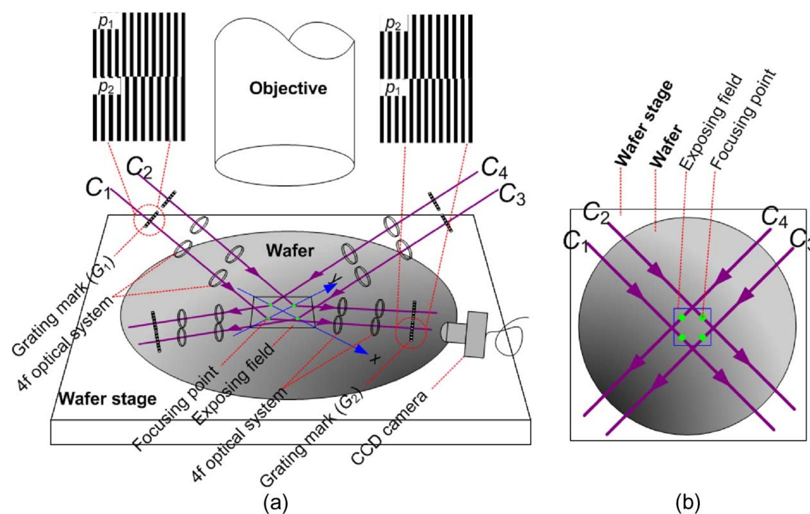

Fig. 2. (a) The space diagram of the four-channel focusing and leveling scheme. (b) The top-view diagram of the scheme.

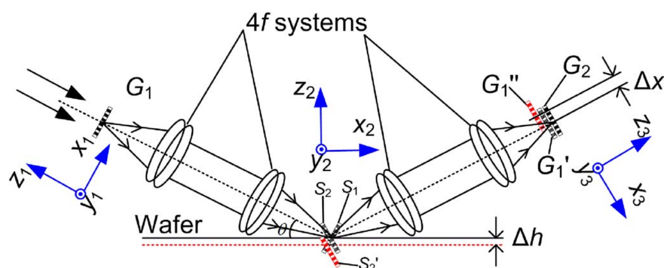

Fig. 3. The diagram of the single-channel optical structure which is composed of two adjacent $4f$ optical systems that establish the connection between G_1 and G_2.

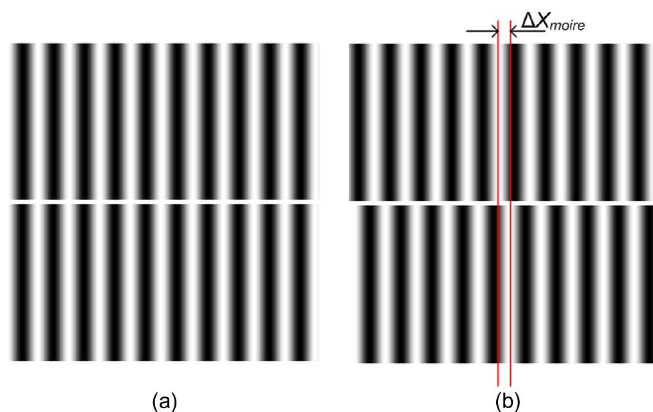

Fig. 4. The moiré fringes formed from superposing G_1' and G_2. (a) The perfectly aligned moiré fringes simulated when the wafer locates at the ideal focal plane. (b) The misaligned moiré fringes caused by wafer defocusing.

red dotted horizontal line in Fig. 3) from the ideal focal plane (the solid horizontal line in Fig. 3), the vertical defocusing amount Δh introduces a transverse shift Δx between G_1'' (an image from S_2') and G_2, which manifests a greatly shift ΔX_{moire} or phase variation $\Delta\varphi_{moire}$ between the upper and lower moiré fringes, shown in Fig. 4(b). Referring to (4) and Fig. 3, the vertical defocusing amount can be derived as

$$\triangle h = \frac{\Delta x}{2\sin\theta} = \frac{1}{2\sin\theta}\frac{\Delta\varphi_{moire}}{2\pi}\frac{p_1 \cdot p_2}{p_1 + p_2} = \frac{1}{2}\frac{\Delta X_{moire}}{2\sin\theta}\left(\frac{|p_1 - p_2|}{p_1} + \frac{|p_1 - p_2|}{p_2}\right). \tag{5}$$

Demodulating the phase variation $\Delta\varphi_{moire}$ or the transverse shift ΔX_{moire} between the moiré fringes, the vertical defocusing amount Δh could be obtained. In the same manner, the defocusing amounts of other three points can be simultaneously obtained as well.

Herein, it seems that the wafer tilts and the central defocusing amount of the wafer could be calculated quite easily with those heights of the four focusing points. However, note that the moiré-based metrology range $(p_1 \cdot p_2)/[2\sin\theta(p_1 + p_2)]$ (Considering a full period phase shift from 0 to 2π in (5), Δh would change from 0 to $(p_1 \cdot p_2)/[2\sin\theta(p_1 + p_2)]$) is just within several micrometers, which indicates the up and down fluctuations at those focusing point may exceed the measuring range with very slight wafer tilts. Considering an exposing field at millimeters level, this slight tilt should be less than 10^{-3} rad to guarantee the wafer fluctuation within the measuring range. Nevertheless, in some exposing fields, the tilt angle may go beyond that. As a consequence, the distributions of designated moiré fringes will not be vertically parallel with each other as shown in Fig. 4(a) and (b) but will be deformed ones, which fatally blocks the extraction of defocusing amount at each focusing point.

To solve those barriers, a tilt detection and remediation strategy is adopted firstly to relocate the wafer into the moiré-based metrology range. Hereafter, the vertical defocusing amount at each focusing point will be precisely extracted by comparing the difference between vertically parallel moiré fringes.

Note that actually, even though the tilt detection and remediation strategy could perfectly level the wafer to horizontal position, the wafer position still can't be distinguished when Δh reaches the value that causes shift of moiré fringes by a full period. To solve this problem, the practical focusing process could be conducted under a coarse-fine focusing strategy. In coarse focusing, a slot or hole like mark is projected onto the central position of an exposing field, and then reflected onto another side to transform the up and down height variation into image shift (this way is similar to reference [6]). The coarse focusing method generally achieves accuracy within 1 μm. Hereafter, the rest fine focusing procedure is all about our moiré-based four-channel scheme. In addition, the triangular coarse focusing method is familiar and mature, and this paper does not discuss it further.

3. Tilt and Defocusing Amount Detections on a Tilted Wafer

Previous derivations has shown that the vertical defocusing amount Δh would result in a transverse shift from G_1' to G_1''. Similarly, if focus on a tilted wafer, the image G_1' in Fig. 3 would represent a deformation of G_1, which indicates that G_1' may not be perfectly superposed with G_2. Since the distributions of moiré fringe is determined by both the tilt-modulated G_1' and the stationary G_2, conclusion can be drawn that the wafer tilts are closely relevant to the phase distribution of the moiré fringes too.

To explore the relationship between wafer tilts and moiré distributions, we'd like to track the shape transforms from G_1 to G_1' on a tilted wafer. In Fig. 3, three Cartesian coordinates are located on the G_1 plane $(x_1 - o_1 - y_1)$, the wafer plane $(x_2 - o_2 - y_2)$ and the G_2 plane $(x_3 - o_3 - y_3)$, respectively. The transforms from G_1 to G_1' can be divided into three steps: coordinate transform from $(x_1 - o_1 - y_1)$ to $(x_2 - o_2 - y_2)$, position transform of specula reflection on the tilted wafer, and coordinate transform from $(x_2 - o_2 - y_2)$ to $(x_3 - o_3 - y_3)$.

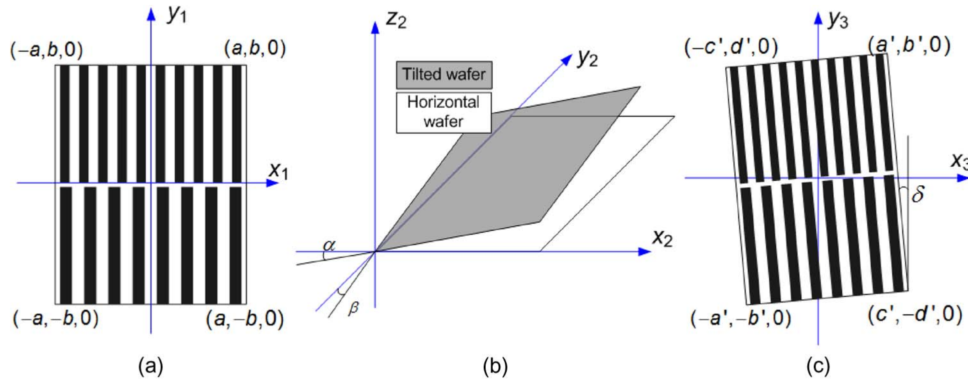

Fig. 5. (a) The original rectangular grating mark G_1. (b) The wafer tilts around x_2 and y_2 axis for angle α and β, respectively. (c) The IPT G_1' caused from wafer tilts.

Coordinate transform between $(x_1 - y_1 - z_1)$ and $(x_2 - y_2 - z_2)$ equals a rotation θ around y_1 axis. The coordinate transform 4×4 mat can be written as

$$R_1 = \begin{pmatrix} \cos\theta & 0 & \sin\theta & 0 \\ 0 & 1 & 0 & 0 \\ \sin\theta & 0 & \cos\theta & 0 \\ 0 & 0 & 0 & 1 \end{pmatrix}. \tag{6}$$

As the wafer deflects from the the ideal focal plane for a small angle α around y_2 axis and angle β around x_2 axis [see Fig. 5(b)], the specula reflection that occurs on the tilted wafer surface can be treated as a position transform between the original point (object point) and its conjugated point (Image point) referring to the tilted wafer. The normal vector of the tilted wafer can be written as $(\cos(\pi/2-\alpha), \cos(\pi/2-\beta), \cos\gamma)$, where $\cos\gamma = \sqrt{1-\cos^2(\pi/2-\alpha)-\cos^2(\pi/2-\beta)}$. Thus, based on these geometric relations, position transform mat of this specula reflection can be expressed as

$$R_2 = \begin{pmatrix} 1-2\sin\alpha\cdot\sin\alpha & -2\sin\alpha\cdot\sin\beta & -2\sin\alpha\cdot\cos\gamma & 0 \\ -2\sin\beta\cdot\sin\alpha & 1-2\sin\beta\cdot\sin\beta & -2\sin\beta\cdot\cos\gamma & 0 \\ -2\cos\gamma\cdot\sin\alpha & -2\cos\gamma\cdot\sin\beta & 1-2\cos\gamma\cdot\cos\gamma & 0 \\ 0 & 0 & 0 & 1 \end{pmatrix}. \tag{7}$$

Furthermore, the coordinate transform between coordinates $(x_2 - y_2 - z_2)$ and $(x_3 - y_3 - z_3)$ performs a rotation θ around y_2 axis. The coordinate transform mat is the same as R_1 mentioned above

$$R_3 = \begin{pmatrix} \cos\theta & 0 & \sin\theta & 0 \\ 0 & 1 & 0 & 0 \\ -\sin\theta & 0 & \cos\theta & 0 \\ 0 & 0 & 0 & 1 \end{pmatrix}. \tag{8}$$

Taking into account a rectangular grating mark G_1 that locates at the $x_1o_1y_1$ plane shown in Fig. 5(a), four corner vertexes are $(a,b,0)$, $(-a,b,0)$, $(a,-b,0)$ and $(-a,-b,0)$, respectively. The transformation from $(x_1 - o_1 - y_1)$ to $(x_3 - o_3 - y_3)$ is achieved by successive transforms of R_1, R_2 and R_3, namely

$$(x_3, y_3, z_3, 1) = (x_1, y_1, z_1, 1)R_1R_2R_3. \tag{9}$$

Consequently, in Fig. 5(c), image G_1' that projected on $x_3o_3y_3$ plane is shown as an IPT shape, which is directly related to wafer tilts α and β. The four corner vertexes are presented by

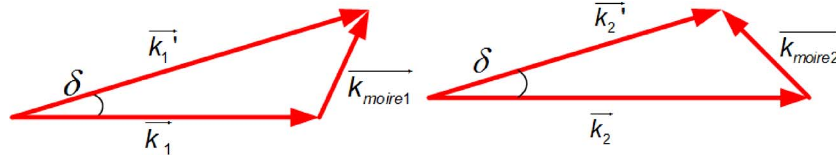

Fig. 6. The vector operation between two superposed gratings.

$(a', b', 0)$, $(-c', d', 0)$, $(c', -d', 0)$, and $(-a', -b', 0)$. According to (9), the coordinates a', b', c', and d' can be deduced from

$$\begin{aligned} b' + d' &= 2b(1 - 2\sin^2\beta) \\ b' - d' &= -4a\sin\theta\cos\gamma\sin\beta \\ a' - c' &= -4b\cos\gamma\sin\beta\sin\theta \\ a' + c' &= 2a(1 - 2\sin^2\alpha)\cos^2\theta + 2a(1 - 2\cos^2\gamma)\sin^2\theta. \end{aligned} \tag{10}$$

Moreover, (1) and (2) indicate that a grating can be described by its transverse vector which consists of the grating period and IPT angle. In Fig. 5(c), the IPT angle δ and period of upper and lower gratings can be derived as

$$\tan\delta = \frac{c' - a'}{b' + d'} = \frac{2\cos\gamma\sin\beta\sin\theta}{1 - 2\sin^2\beta} \approx 2\sin\beta\sin\theta \tag{11}$$

$$p' = p\frac{\sqrt{(a' + c')^2 + (b' - d')^2}}{2a} \approx p \cdot \cos(2a) \tag{12}$$

where, p is the original periods of G_1. Considering that the focusing and leveling processes are always conducted on a precise wafer stage, one can feasibly suppose that the wafer tilts α and β are within 1° (0.0174 rad). Therefore, (11) can be approximately written as $\delta = 2\sin\beta\sin\theta$, on the basis of that $\cos\gamma/(1 - 2\sin^2\beta) = 1.0003 \approx 1$ $(\alpha = \beta = 1°)$. In addition, in (12), the periods of upper and lower gratings are compressed by a ratio $\cos(2\alpha)$ that is more than 0.9994, which means the periods of gratings G_1' decrease very slightly. The transverse vector of upper and lower gratings in G_1' [see Fig. 5(c)] can be written as

$$\overrightarrow{k_1}' = \frac{2\pi}{p_1 \cdot \cos(2\alpha)}\exp(i\delta) \tag{13}$$

$$\overrightarrow{k_2}' = \frac{2\pi}{p_2 \cdot \cos(2\alpha)}\exp(i\delta). \tag{14}$$

Superposing the tilt-modulated G_1' and stationary G_2, the transverse vectors of the moiré fringes can be determined by the vector operation as shown in Fig. 6, where $\overrightarrow{k_1} = (2\pi/p_2)\exp(j0)$ and $\overrightarrow{k_2} = (2\pi/p_1)\exp(j0)$ are the upper and lower transverse vectors of gratings in G_2. Apparently, the directions of $\overrightarrow{k_{moire1}}$ and $\overrightarrow{k_{moire2}}$ will change along with the IPT angle δ which is directly relevant with the wafer tilt β [see (11)]. In other words, to determine the wafer tilt β, the relationship between moiré distributions and the IPT angle δ should be addressed. According to Equations (11)–(14) and Fig. 6, the included angle (η_{moire}) between $\overrightarrow{k_{moire1}}$ and $\overrightarrow{k_{moire2}}$ can be expressed as

$$\eta_{moire} = \arctan\left(\frac{f_1\sin\delta\cos(2\alpha)}{f_1\cos\delta\cos(2\alpha) - f_2}\right) - \arctan\left(\frac{f_2\sin\delta\cos(2\alpha)}{f_2\cos\delta\cos(2\alpha) - f_1}\right). \tag{15}$$

In (15), two factors (the IPT angles δ and wafer tilt α) could influence η_{moire}. We'd like to investigate them successively. In Fig. 7(a), four pairs of moiré fringes are simulated [referring to (2)]

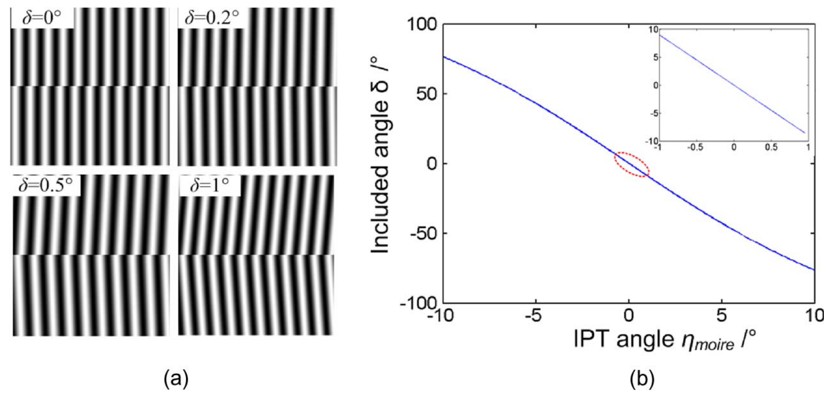

Fig. 7. (a) Moiré fringes generated with different IPT angles δ, i.e. 0°, 0.2°, 0.5° and 1°, respectively. (b) The correlogram between included angle and IPT angle, while α is set to be 0°.

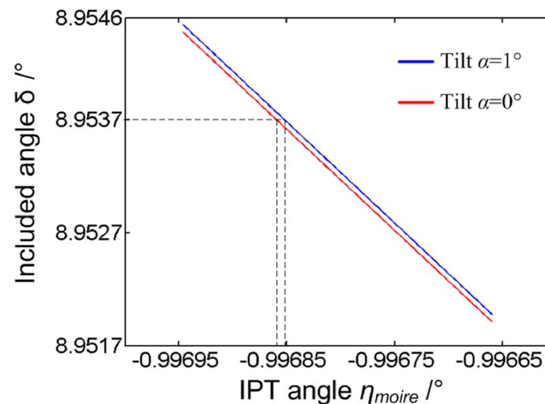

Fig. 8. The locally zoomed curves of included angles plotted at $\alpha = 0°$ and $\alpha = 1°$.

from superposing G_1' and G_2 with different δ to intuitively illustrate the deformed moiré distributions. As δ increases, the vertically parallel moiré fringes become tilted with each other. Furthermore, the quantitative conversion curve involving included angle and IPT angle is plotted in Fig. 7(b) according to (15). Evidently, a tiny IPT angle would result in a seven times larger included angle. Particularly, within a small range from $-1°$ to 1°, the curve tends to be linear, shown in the upper right sub-graph.

As to the wafer tilt α, considering a specific positive or negative α in (15), the upper and lower moiré fringes would rotate clockwise or anticlockwise simultaneously. Fig. 8 shows two correlograms between included angle and IPT angle plotted at $\alpha = 0°$ and $\alpha = 1°$. With the same included angle, an extremely tiny error is introduced by α. Therefore, it is reasonable to announce the included angle η_{moire} is only sensitive to the IPT angle δ while independent from the wafer tilt α around the y_2 axis.

Applying a phase demodulation algorithm on the designated moiré fringes, the included angle η_{moire} could be detected with a preserved accuracy at 10^{-3} rad, and then the accuracy of IPT angle δ could be achieved with accuracy at 10^{-4} rad. Referring to (11), the tilt angle β around x_2 axis could be obtained precisely.

Combine the four-channel focusing scheme in Fig. 2, the tilt angle around x axis can be figured out by C_1 and C_2, and the tilt angle around y axis can be detected by C_3 and C_4. Remedy these tilts, on one hand, the defocusing amounts of four focusing points could fluctuate in the range of micrometer, which is within the moiré-based metrology range; on the other hand, the moiré fringes would display straightly without included angle. Then, vertical defocusing

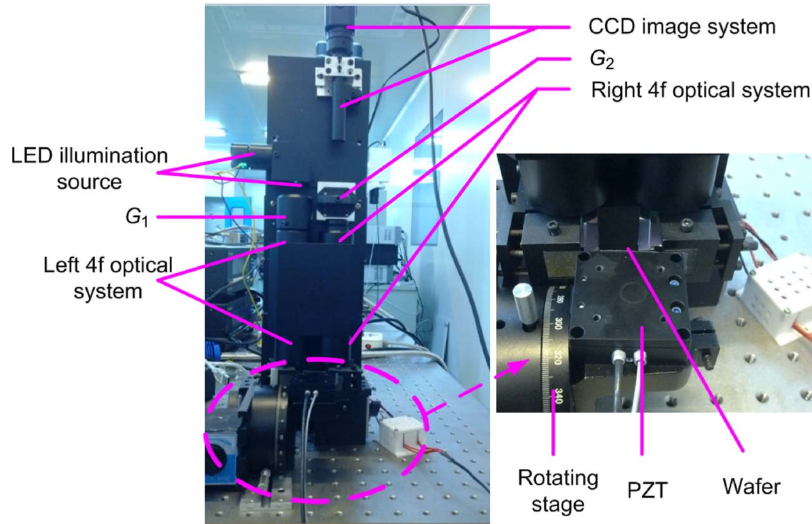

Fig. 9. The experimental setup.

amount extracted at each focusing point can be accomplished by calculating transverse shift (see Fig. 4) between two sets of vertically parallel moiré fringes.

4. Experiments and Discussions

To experimentally confirm the four-channel focusing and leveling scheme in a proof-to-concept way, an experimental setup for the single-channel focusing scheme is constructed as illustrated in Fig. 9. The incident planar wave is generated by collimating the LED illumination source with main wavelength 530 nm and spectral bandwidth 30 nm. The periods of upper and lower gratings of G_1 (binary amplitude type) are 8 μm and 10 μm, respectively, while periods of G_2 (also, binary amplitude type) are 10μm and 8μm. Under G_1, the left 4f system is vertically placed, which images G_1 onto the wafer that pasted on a piezoelectric translator (PZT, the resolution and stroke are 2 nm (closed loop) and 200 μm, respectively). The PZT is fixed on the rotating stage. Associating the rotating stage with PZT, both rotation and straight movements can be implemented. By two symmetrically distributed 4f systems, the image of G_1 is finally imaged (at 80° incident angle) onto the G_2 plane, where two sets of moiré fringes emerged from the superposed gratings structures. Behind G_2, an imaging lens is introduced to image the moiré fringes onto the CCD target surface. The focal length, NA and magnification of this lens are respectively 110 mm, 0.041 and 8$\times$. Hereafter, the moiré fringes are captured by the CCD (WAT902H2, China. 768 $\times$ 576 with pixel width of 10 μm. The whole system is carefully adjusted to achieve a uniform illumination and clear moiré fringes on the CCD camera.

During one experiment, the wafer locates at the position that is near both the back focal plane of left 4f system and the front focal plane of the right 4f system. The captured moiré fringes (smoothed by the low NA imaging lens and median filter in the image acquisition software) appear as shown in Fig. 10(a) and its cross-sections of the intensity distributions are shown in Fig. 10(b). The cross-sections manifest as analogous sine-distributions while the contrasts variation may cause from slightly non-uniform illumination. Applying a 2-D Fourier transform on the upper and lower set moiré fringes, two phase maps respectively termed as $F_1(x, y)$ and $F_2(x, y)$ are displayed in Fig. 10(c). The directions of transverse vectors $\overrightarrow{k_{moire1}}$ and $\overrightarrow{k_{moire2}}$ are in accord with the phase gradients. At every pixel point (x_0, y_0), the corresponding gradient is

$$\nabla F(x_0, y_0) = \frac{\partial F}{\partial x}\vec{i} + \frac{\partial F}{\partial y}\vec{j}\bigg|_{x=x_0, y=y_0} \qquad (16)$$

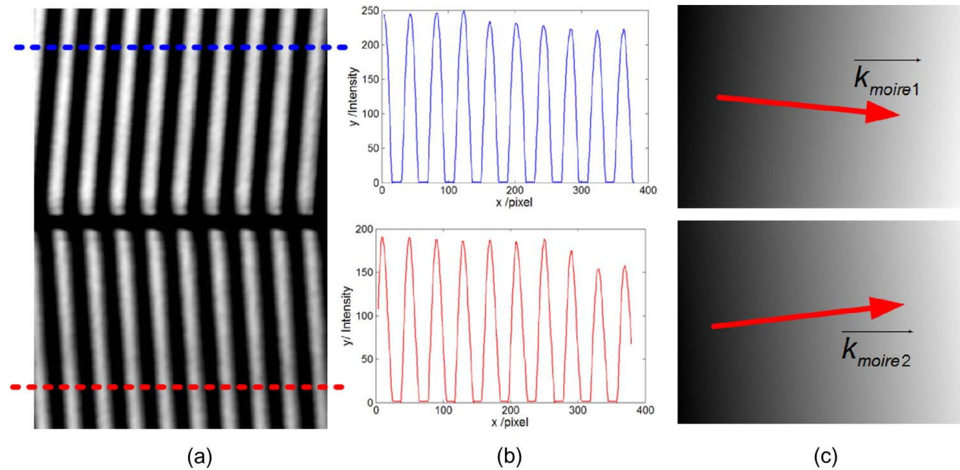

Fig. 10. (a) The moiré fringes captured during experiment. (b) The analogous sine-distributions of the red and blue dotted rows in Fig. 10(a). (c) The phase distributions of moiré fringes.

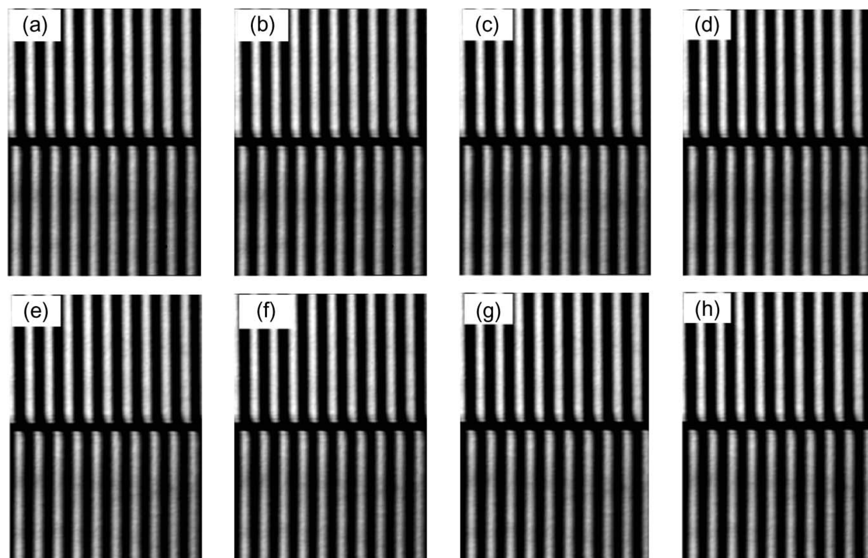

Fig. 11. The moiré fringes with 200 nm step length between adjacent images.

where, $\partial F/\partial x$ is the partial derivatives in x directions, and $\partial F \partial y$ is the partial derivative in the y direction.

In Fig. 10(c), the upper and lower average phase gradients are calculated as $0.113 - 0.00908i$ and $0.112 + 0.0072i$, respectively. Consequently, the included angle of $\overrightarrow{k_{moire1}}$ and $\overrightarrow{k_{moire2}}$ is figured as 8.292°. And the wafer tilt β around x_2 axis (see Fig. 5) can be derived from Eq. (15) and (11) as 0.468°.

Adjust the wafer plane via the rotating stage for 0.468° around x_2 (see Fig. 3) axis, two sets of vertical moiré fringes, without included angle, are presented in Fig. 11(a). Obviously, the upper moiré fringes don't align with the lower ones, which indicates that the wafer defocuses from the ideal focal plane. To verify the vertical focusing performance, the PZT is adopted to perform the step movement along the x_2 (see Fig. 3) axis. Several sets of moiré fringe images are recorded with different step lengths, i.e., 50 nm, 100 nm, and 200 nm. To be convenient, the images with step length 200 nm are given in Fig. 11(a)–(h).

TABLE 1
The calculated and theoretical defocusing amounts of moiré fringes in Fig. 11 (in microns)

Calculated	0.732	0.934	1.131	1.333	1.536	1.739	1.935	2.137
theoretical	0.732	0.932	1.132	1.332	1.532	1.732	1.932	2.132

In Fig. 11, the transverse shift or phase difference (between upper and lower moiré fringes) enlarges with the PZT movement. Set Fig. 11(a) as a reference position, defocusing amounts are calculated from the phase differences according to Eq. (5). In Table 1, defocusing amounts in both calculated and theoretical cases are tabulated for comparison.

From those calculated data, the maximal error, mean error and standard deviation, are sorted out as 0.007 μm, 0.0026 μm and 0.00267 μm, respectively. Similarly, the corresponding results, with step length 50 nm and 100 nm, are calculated as 0.003 μm, 0.000625 μm, 0.001598 μm, and 0.005 μm, 0.0016 μm, 0.00238 μm. These results directly prove that the defocusing amount detection can achieve a high accuracy at nanometers level.

As expected, the moiré-based measurement method expresses high performances in both tilt detection and defocusing extraction. The main reason for this is that the measurands including IPT angle and vertical defocusing amount can be derived from the several times larger corresponding included angle and moiré fringe shift. The negligible errors might be from environmental disturbance, algorithm error and PZT step error.

Still, it should be noted that above experiments and discussions are related to a single-channel focusing structure. Not withstanding its limitation, if a four-channel focusing and leveling mechanism like previously described in Fig. 2 is given, the focusing and leveling processes may follow three steps, i.e., firstly, remedy the wafer tilt around x axis with the angle calculated from channels C_1 and C_2, as well as the wafer tilt around y axis from channels C_3 and C_4 (we name this step pre-tilt remediation, and it is often performed by three points mechanical divers); secondly, defocusing amounts at four focusing points can be determined from the parallel distributed moiré fringes in each channel; finally, the central height of wafer can be presented by the mean height of all four channels, and a second-tilt remediation between four points will usually be achieved by the ultrahigh precise piezoelectric motors.

5. Summary

To summarize, a moiré-based four-channel focusing and leveling scheme is presented. The detections of wafer tilts as well as the vertical defocusing amount that are encoded in the phase distributions of moiré fringes are studied. Results demonstrate that, with a single-channel focusing structure, the wafer tilt around x_2 axis can be firstly remedied by calculating the included angle between moiré fringes. Also, the vertical defocusing amount with accuracy at nanometers level can be detected by comparing the phase difference between vertically parallel moiré fringes. Additionally, in a practical four-channel focusing application, the focusing and leveling processes could be accomplished in another three steps mentioned above, i.e. pre-tilt remediation, heights extraction of four points and second-tilt remediation.

Acknowledgment

The authors thank D. Yin and Y. Tang for their helpful assistance during experiment and discussion in writing this paper, as well as the anonymous reviewers for their valuable suggestions.

References

[1] I. Mori *et al.*, “Selete's EUV program: progress and challenges,” in *Proc. SPIE Adv. Lithogr.*, vol. 6921, Mar. 2008, pp. 692102-1–692102-12.
[2] F. Kahlenberg *et al.*, “Best focus determination: bridging the gap between optical and physical topography,” in *Proc. SPIE Adv. Lithogr.*, vol. 6520, Mar. 2007, pp. 65200Z-1–65200Z-8.

[3] M. Pike *et al.*, “Effects of intra chip topography in back end of line processes on focus leveling control and process window degradation with high NA exposures,” in *Proc. IEEE Adv. Semicond. Manuf.*, May 2004, pp. 75–78.

[4] Z. Shi, V. Kochergin, and F. Wang, “193 nm Superlens imaging structure for 20 nm lithography node,” *Opt. Exp.*, vol. 17, no. 14, pp. 11 309–11 314, Jul. 2009.

[5] M. Mellier *et al.*, “Full copper electrochemical mechanical planarization (Ecmp) as a technology enabler for the 45 and 32 nm nodes,” in *Proc. IEEE Int. Interconnect Technol. Conf.*, Jun. 2007, pp. 70–72.

[6] K. Suwa and K. Ushida, “The optical stepper with a high numerical aperture i-line lens and a field-by-field leveling system,” in *Proc. SPIE Int. Symp. Microlithogr.*, Jan. 1988, vol. 0922, pp. 270–276.

[7] K. Suzuki, S. Wakamoto, and K. Nishi, “KrF step-and-scan exposure system using higher-NA projection lens,” in *Proc. SPIE Int. Symp. Microlithogr.*, vol. 2726, Jun. 1996, pp. 767–779.

[8] T. Hagiwara *et al.*, “Wafer edge-shot algorithm for wafer scanners,” in *Proc. SPIE Int. Symp. Microlithogr.*, vol. 4691, Jul. 2002, pp. 790–801.

[9] H. Kawashima and A. Suzuki, “Method and apparatus for precisely detecting surface position of a patterned wafer,” U.S. Patent 5 118 957, Jun. 2, 1992.

[10] D. C. Flanders and T. M. Lyszczarz, “A precision wide-range optical gap measurement technique,” *J. Vac. Sci. Technol. B, Microelectron. Nanom. Struct.*, vol. 1, no. 4, pp. 1196–1199, Oct. 1983.

[11] Y. Oshida, M. Tanaka, T. Tanimoto, and T. Kurosaki, “Chip leveling and focusing with laser interferometry,” in *Proc. SPIE Int. Symp. Microlithogr.*, Jun. 1990, vol. 1264, pp. 244–251.

[12] K. Kato, T. Itoh, and N. Atoda, “A new optical heterodyne alignment and gap detection technique for x-ray steppers,” *Microelectron. Eng.*, vol. 23, no. 1, pp. 185–188, Jan. 1994.

[13] J. E. Van Der Werf, “Optical focus and level sensor for wafer steppers,” *J. Vac. Sci. Technol. B, Microelectron. Nanom. Struct.*, vol. 10, no. 2, pp. 735–740, Mar. 1992.

[14] W. Yan, Y. Yang, W. Chen, S. Hu, and S. Zhou, “Moiré-based focusing and leveling scheme for optical projection lithography,” *Appl. Opt.*, vol. 49, no. 31, pp. 5959–5963, May 2010.

[15] S. Zhou *et al.*, “Moiré-based phase imaging for sensing and adjustment of in-plane twist angle,” *IEEE Photon. Tech. Lett.*, vol. 25, no. 18, pp. 1847–1850, Sep. 2013.

[16] S. Zhou *et al.*, “Fourier-based analysis of Moiré fringe patterns of superposed gratings in alignment of nanolithography,” *Opt. Exp.*, vol. 16, no. 11, pp. 7869–7880, May 2008.

[17] J. Ruan and J. Hartley, “An innovative design of wafer height and tilt sensor for lithography systems,” *J. Vac. Sci. Technol. B, Microelectron. Nanom. Struct.*, vol. 26, no. 6, pp. 2043–2048, Dec. 2008.

[18] V. Ray, Y. Aida, R. Funakoshi, H. Kato, and S. W. Pang, “High resolution patterning on nonplanar substrates with large height variation using electron beam lithography,” *J. Vac. Sci. Technol. B, Microelectron. Nanom. Struct.*, vol. 30, no. 6, pp. 06F303-1–06F303-7, Nov. 2012.

[19] E. van West, A. Yamamoto, and T. Higuchi, “Manipulation of thin objects using levitation techniques, tilt control, and hapics,” *IEEE Trans. Autom. Sci. Eng.*, vol. 7, no. 3, pp. 451–462, Jul. 2010.

[20] J. W. Goodman, and S. C. Gustafson, “Introduction to Fourier optics, second edition,” *Opt. Eng.*, vol. 35, no. 5, p. 1513, May 1996.

[21] O. Bryngdahl, “Moiré: Formation and interpretation,” *J. Opt. Soc. Amer.*, vol. 64, no. 10, pp. 1287–1294, Oct. 1974.

[22] Y. S. Ku, D. M. Shyu, Y. S. Lin, andC. H. Cho “Infrared differential interference contrast microscopy for 3D interconnect overlay metrology,” *Opt. Exp.*, vol. 21, no. 16, pp. 18 884–18 898, Aug. 2013.